Predictive Engineering Model for Life and Performance Assessment of High-Power Electric Propulsion Systems

IEPC-2022-410

Presented at the 37th International Electric Propulsion Conference
Massachusetts Institute of Technology, Cambridge, MA USA
June 19-23, 2022

Richard E. Wirz[1]
University of California, Los Angeles, CA, 90095, USA

Alex A. Gorodetsky[2], Benjamin A. Jorns[3]
University of Michigan, Ann Arbor, MI, 48109

Mitchell L. R. Walker[4]
Georgia Institute of Technology, Atlanta, GA 30332

The Joint AdvaNced PropUlsion InStitute (JANUS) is using a Predictive Engineering Model (PEM) framework to assess the life and performance of NASA's high-power electric propulsion systems. The primary challenge for accurate assessment is accounting for the relatively extreme facility effects encountered during ground-based testing of high-power, high-flowrate EP devices. The Predictive Engineering Modeling (PEM) framework utilizes a combination of multi-fidelity, multi-physics models of physical processes with models of the propulsion system, environment, and power electronics to assess thruster performance and life. These models work together with a governing PEM framework to provide integrated, holistic simulations of the system behavior in different vacuum facilities. Differences between the facility and in-space behavior, and optimization efforts to reduce these differences, are used to inform facility effect mitigation strategies. Uncertainty quantification (UQ) will provide probabilistic extrapolations to in-space performance and life, and feedback to guide experimental and high-fidelity simulation campaigns needed to improve model accuracy. As such, the PEM provides a multi-disciplinary and multi-participant framework for making significant progress towards confidently predictive the life and performance of high-power EP systems.

[1] Professor, Mechanical & Aerospace Engineering, wirz@ucla.edu, AIAA Associate Fellow.
[2] Assistant Professor, Aerospace Engineering, goroda@umich.edu, AIAA Member.
[3] Assistant Professor, Aerospace Engineering, bjorns@umich.edu, AIAA Member.
[4] Professor, Aerospace Engineering, mitchell.walker@ae.gatech.edu, AIAA Associate Fellow.

I. Introduction

The Joint AdvaNced PropUlsion InStitute (JANUS) was recently created under the NASA Space Technology Research Institute program with the is to enable and proliferate the flight of high-power electric propulsion (EP) systems [1]. In particular, JANUS will utilize physics-based modeling, high-power thruster testing, novel diagnostic development, and fundamental experiments to advance mitigation strategies to overcome the uncertainties of life and performance prediction associated with ground testing capabilities.

II. Approach

Figure 1 illustrates key elements and interrelationships of JANUS. These tiers are categorized into institutional initiatives of Performance and Life Assessment, Thruster Environment Studies, and Fundamental Studies. Since high-power EP facility effects are governed temporally and spatially by multi-scale phenomena, the Fundamental Studies will provide higher fidelity while the Coupled System Studies and Performance and Life Assessment provide greater scope to capture the behavior of the overall system. As described in the following sections, the Fundamental Studies reduce critical uncertainties (*i.e.*, yields, cross-sections, etc.) based on critical physical processes via reduced-order Sub-Models that must be used for the thruster, plume, and environment System Models developed in the Thruster Environment Studies. These coupled System Models comprise the Predictive Engineering Model (PEM) that is used to predict thruster performance and life for test or mission profiles in specified environments (*i.e.*, inside a specified ground facility or spacecraft/in-space environment). The priorities of the efforts within these initiatives are guided by Uncertainty quantification (UQ).

The overall objective of the Modeling Framework is to ensure that the PEM and its associated models will accurately quantify ground-test facility impacts on high-power EP systems. The UQ feedback will systematically ensure JANUS undertakes coordinated efforts that provide the highest payoff towards this objective. By comparing the results between different ground tests and in-space, the PEM can be used to quantitatively assess the ground-test facility designs, methodologies, and procedures that most effectively mitigate facility effects. The following sections describe this framework and the associated models.

The PEM, which we denote as

$$PEM\left(\vec{H}\left(\vec{X}(t);\vec{\Theta}\right)\right)$$

is a function that yields model predictions of the thruster performance and life in a prescribed environment, $\vec{Y}_{T,E}$. Examples of components of $\vec{Y}$ include global parameters such as performance (e.g., thrust, specific impulse, efficiency) and lifetime, as well as spatially distributed properties like the plume profiles, species/contaminant fluxes, and temporal properties such as thruster stability. The function PEM iteratively determines the coupled effects of the thruster, plume, and environment System Models

$$\vec{H} = (H_T, H_P, H_E, H_{T-P}, H_{P-E})$$

where H_{T-P} and H_{P-E} describe the coupling functions between the respective models. Not shown in the figure is electrical power system (pwr) coupling that will inform additional coupling functions H_{pwr-T} and H_{E-pwr} for power system to thruster, and environment to power system, respectively, thus closing the thruster-environment circuit. Inputs to $\vec{H}$ include system parameters, $\vec{X} = \left(\vec{X}_T, \vec{X}_E\right)$ such as thruster life, throttle conditions, and the facility environment, and model parameters, $\vec{\Theta} = (\Theta_1, \Theta_2, \Theta_3, \dots)$ such as sputtering yield coefficients and electron transport diffusion terms. The system parameters are quantities that can be controlled for the thruster, $\vec{X}_T$, e.g., thruster geometry and throttle condition (flow rate, voltage, current, magnetic field setting), as well as the environment, $\vec{X}_E$, e.g., pump location and speed, material liner, and electrical configuration. For in-space operation, $\vec{X}_E$ will describe the orbit environment, spacecraft structure, and surfaces. In the absence of a thruster System Model or in the presence of reliable plume data, one may use detailed descriptions of the plume produced by the thruster, $\vec{X}_P$, as measured via ground-test plume measurements in addition to or in place of thruster inputs. This allows the PEM to estimate the performance of less-developed thruster technologies, such as MPDTs and FRCs, without detailed thruster models. The model parameters, $\vec{\Theta}$, and their use and characterization in the context of the Modeling Framework are described in the Exemplar Projects.

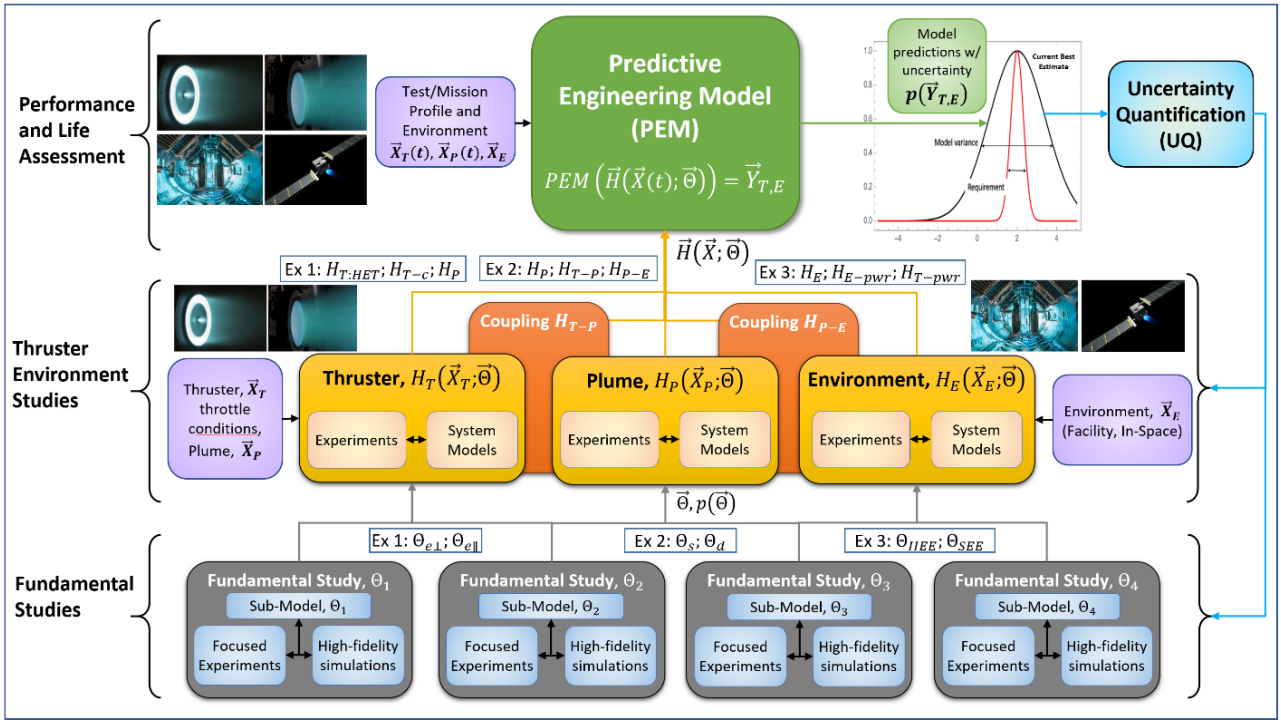

Figure 1: Predictive Engineering Model (PEM) integrated into the framework for the JANUS project.

An example of the PEM for ion thrusters is shown in Figure 2. The PEM takes a test or mission profile, $\vec{X}_T(t), \vec{X}_P(t)$, and the operational environment, $\vec{X}_E$, and iterates through the profile to determine a time history of thruster performance. For each time step, the PEM determines the temporal evolution of life mechanisms and uses a life metric assessment to determine if the thruster has reached end-of-life (EOL) during that time step. Figure 2 uses the example of grid erosion of an ion thruster as the life mechanism and electron backstreaming (EBS) limit as the life metric assessment to determine EOL conditions. An example of this approach is given in Section IV following the NSTAR performance and life modeling effort by Wirz, et al. [2, 3, 4, 5]. For the PEM to develop a probabilistic distribution for a mission, it will also iterate on key conditional probability distributions for system model inputs such as model parameters related to key physical processes, $\vec{\Theta}$, and irreducible sources, indicated by $\vec{\gamma}$.

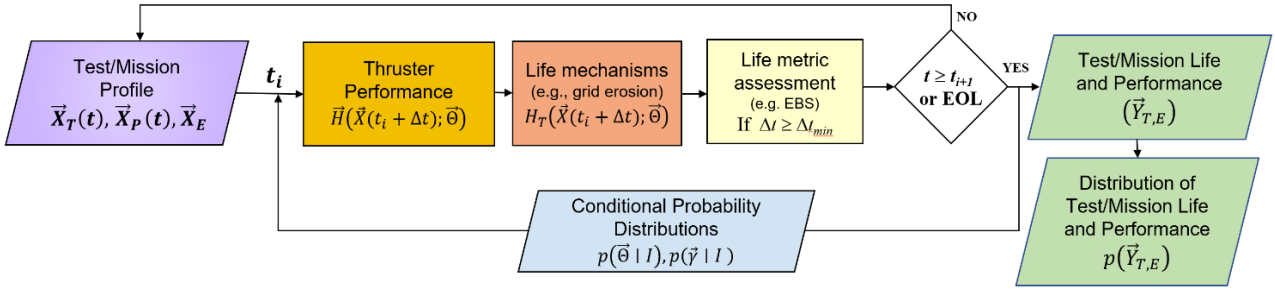

Figure 2: Predictive Engineering Model (PEM) iterative framework. This example shows ion thruster life and performance modeling.

The uncertainty quantification (UQ) framework, shown Figure 3, is responsible for analyzing and providing feedback based on results from the PEM and the feedback that can be associated with the contributing System Models and Sub-Models. Specifically, the primary role of UQ is to use the PEM to develop probabilistic extrapolations of in-space thruster performance and life for a specific set of thruster and facility configurations. The UQ approach will also provide feedback to the PEM by identifying sources of uncertainty that contribute to the greatest variability in predictions and suggesting new investigations to gain information. By exercising this feedback loop, we will target the

refinement of the PEM towards the goal of improved-confidence predictions.

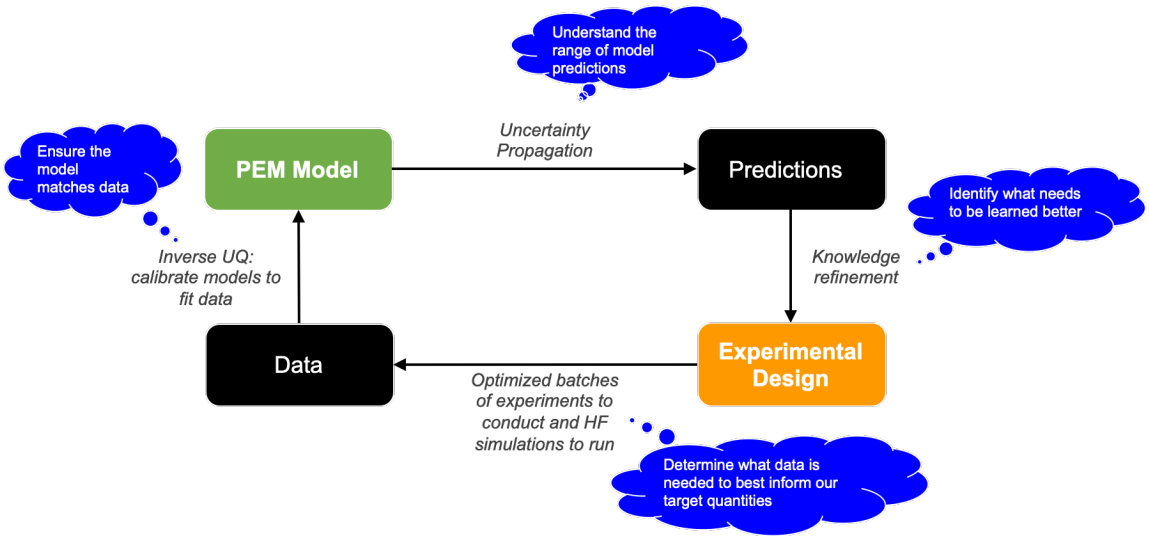

Figure 3: Uncertainty Quantification framework.

Armed with $PEM\left(\vec{H}\left(\vec{X}(t);\vec{\Theta}\right)\right)$, we can generate predictions of thruster performance and life for combinations of design and model parameters. The goal is to find predictions for key operating conditions of the thruster, $\vec{Y}_{T,E}$, given an operating profile, $\vec{X}_T(t)$, and environmental configuration, $\vec{X}_E$,. For simplicity, we can assume that the thruster's plume is determined from the thruster condition and environment, e.g.,

$$(\vec{X}_P\left(\vec{X}_T(t),\vec{X}_E\right)$$

such that the prediction for the thruster performance and life is

$$PEM\left(\vec{H}\left(\vec{X}_T(t)\,,\vec{X}_E;\vec{\Theta}\right)\right) = \vec{Y}_{T,E}.$$

Because there is uncertainty in the models and model parameters, $\vec{\Theta}$, the PEM model predictions will have uncertainty. Additional uncertainty may also stem from irreducible sources related to the environment, γ_1, manufacturing tolerances, γ_2, and the like, that can be represented collectively by $\vec{\gamma} = (\gamma_1, \gamma_2, \ldots)$. The uncertainties in these parameters are expressed as prior distributions $p(\vec{\gamma} \mid I)$ and $p\left(\vec{\Theta} \mid I\right)$, where I denotes the information available at the time of analysis (incorporates all prior available data). The uncertainty in these model parameters directly impacts the confidence of the model predictions from the PEM. The prior predictive distribution is marginalized over the model parameter prior distributions.

The prior predictive distribution can be leveraged to yield probabilistic predictions for the in-space environment. This is the black line in the upper right-hand corner of Figure 4. The largest point represents the most probable predicted state while the width is a direct consequence of inherent model uncertainty. Given our imperfect knowledge of the models for how thrusters respond to facility effects, the uncertainty in the predictions will be larger than a mission-level requirement (the red distribution in Figure 1). One of the overarching goals of JANUS is to reduce this uncertainty. Improving PEM Model confidence can be accomplished in two ways. The first method (system-level), second tier of Figure 1, is based on performing dedicated fundamental studies to narrow the prior model parameter distributions, $p\left(\vec{\Theta} \mid I\right)$. a shows an example of this for a sub-model for the sputtering yield for xenon impacting on Al. We start with a wide marginalized probability distribution for one of the model parameters for the sputtering data. Targeted experiments and detailed studies are used to improve confidence in the model parameters in strategic regions of interest. This process yields a narrower distribution and a more confident prediction by the overall PEM.

The second method (fundamental studies), bottom tier of Figure 1 and , is to perform studies of the thruster at its design state, $\vec{X}_T(t)$, while we vary the facility environment to n set points, $\vec{X}_{E(i)}$ (e.g., pumping speed or electrical boundary condition), and measure the thruster operation at these states, $\vec{Y}_{E(i)}$. This generates a dataset of new information,\

$$\vec{D} = \{ (\vec{X}_{E(1)}, Y_{E(1)}), (\vec{X}_{E(2)}, Y_{E(2)}), \ldots, (\vec{X}_{E(n)}, Y_{E(n)}) \}.$$

We then can apply Bayesian inference to generate a posterior probability distribution function,

$$p(\vec{Y}_{T,E}|\vec{D}) = \int p\left(\left(\vec{Y}_{T,E} \,|PEM, \vec{\Theta}, \vec{\gamma} \right) p(\vec{\Theta} \mid \vec{D}) p(\vec{\gamma} \mid \vec{D}) d\vec{\Theta} d\vec{\gamma}, \text{ where } p(\vec{\Theta} \mid \vec{D}) \right.$$

denotes the posterior distribution of model parameters inferred from the dataset. The posterior probability distribution yields an updated prediction for the model output that has been informed by new, system-level data. This distribution is then sampled (Figure 4) to yield a median prediction (denoted as a black line) and confidence intervals (denoted as dashed lines) as a function of facility environment. Fundamentally, this approach can be thought of as a form of multi-dimensional regression where we have rigorously accounted for sources of uncertainty in evaluating the "goodness of fit."

For both approaches to improve PEM uncertainty, it will be necessary to perform time intensive experiments and simulations. We will use the UQ results to provide feedback to the System Models to quantitatively determine the model parameters, Θ_i, that contribute the greatest uncertainty to the results of the PEM. The JANUS team will coordinate efforts and resources within the pillars to focus on the sub-model uncertainties that are the dominant contributors to PEM uncertainty.

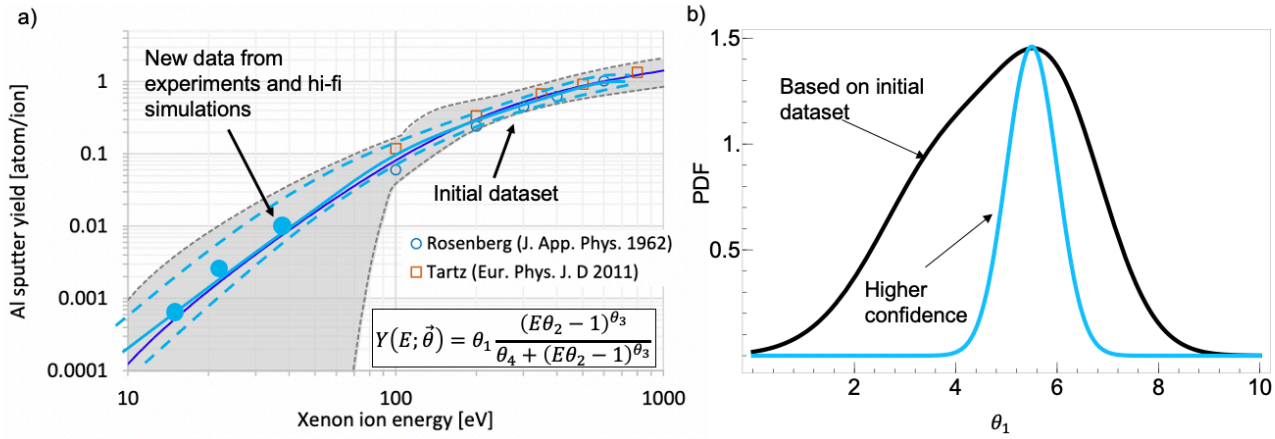

Figure 4: Fundamental studies applied to reduce uncertainty in sub-model parameters. a) Sputtering yield data [6] for Xe on Al. Best fit line is a sub-model based on the Eckstein formula. Model confidence denoted by dashed lines. b) Marginal probability distribution for one of the model parameters before and after additional data is collected.

Simple sampling-based UQ methods will not work because generating priors and posteriors can require 10,000s of runs of the underlying PEM to converge. In our case, some of our constituent models, such as HPHall, may require hours to converge. Instead, Co-I Gorodetsky has developed a cohesive multi-fidelity UQ setting in the context of both sampling and surrogate methodology [7-8, 9] to yield accurate estimates for probability distributions at a fraction of the computation expense. The sampling methods leverage correlations amongst model ensembles, and the surrogate methods leverage localized mappings between each model. The UQ effort will leverage the Dakota Framework, a proven tool for multi-fidelity modeling initiatives. Co-I Gorodetsky works with Dakota developers to add support for these methods and has independent software for performing these analyses within JANUS.

III. Comparing Ground and In-Space Thruster Operation

Comparing ground and in-space thruster behavior requires models that integrate the thruster with the environment. For JANUS, many Co-Is and their researchers must remotely work together to integrate multi-fidelity and multi-physics models and data between institutions. To enable multi-investigator interactions, we have adopted a control volume PEM approach. As shown in Figure 5, the thruster system and facility can be broken up into control volumes that define different regions, regimes, and scales of the governing physics. The coupled system models for this case is

$$\vec{H}_{T,E:f} = H_{T-P}; H_{P-E:f}; H_{E:f-pwr}; H_{pwr-T}$$

where $\vec{H}_{T,E:f}$ indicates thruster T in the environment E of facility f, and employs the coupled System Models for the thruster, plume, environment(facility), and power system. Using this approach, thruster modelers can interface with the plume modelers at the thruster-plume boundary as defined by H_{T-P}. In this example, and as detailed in Figure 6 the thruster and plume model coupling, in both directions, is defined by agreement between the thruster and plume modeling teams. The thruster team may need input from PMI modelers to determine the erosion and transport of sputtered material and secondary electrons. Similarly, the plume model must interact with the PMI modelers at the facility surfaces and beam targets to determine the flux of material and electron from these surfaces. Similar considerations will need to be given for facility coupling with the power, vacuum pumping, CEX plume behavior, cathode plume coupling, and so forth.

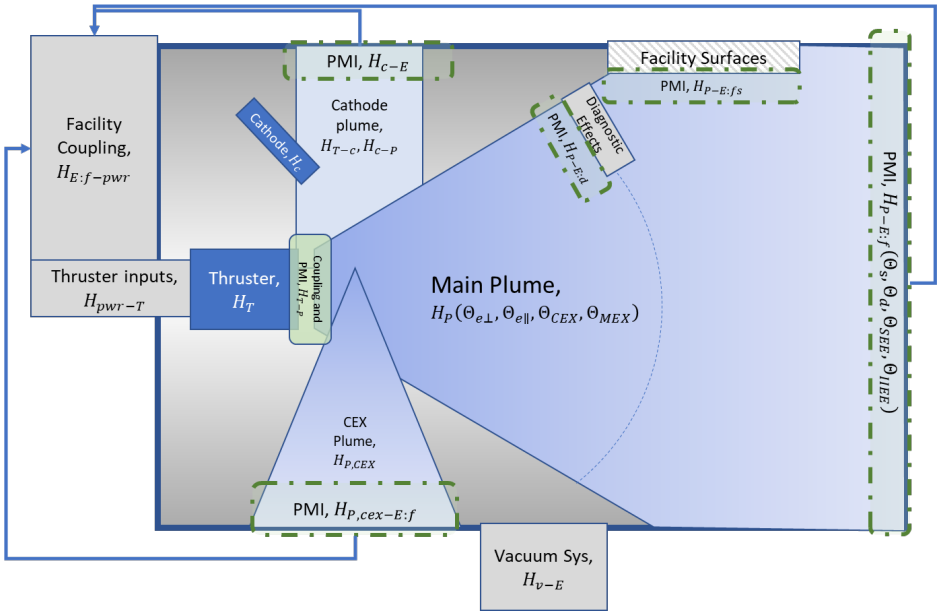

Figure 5: CV discretization of models as applied to ground vacuum facility testing of an EP device.

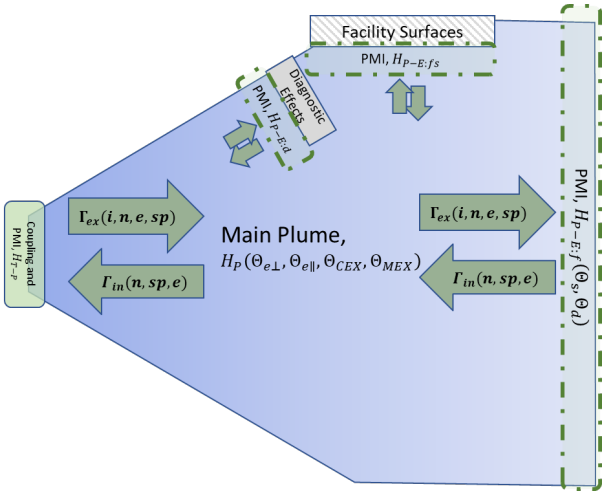

Figure 6: Plume CV showing fluxes due to PMI at surfaces. Additional inputs to this model will include interactions with the CEX plume, cathode, and vacuum system.

Similarly, the CV approach can be applied to the space environment E: sp as shown in Figure 7. In this way, system and coupling modeling efforts for the facilities can be utilized and modified for the space environment, resulting in the coupled system models defined by

$$\vec{H}_{T,E:f} = H_{T-P}; H_{P-E:sp}; H_{E:sp-pwr}; H_{pwr-T}$$

The figure of merit for the ability of a given facility environment $E{:}\,f$ approximates a space environment $E{:}\,sp$ for a thruster T can be determined by comparing the relative performance and life estimates $\vec{Y}_{T,E}$ from the PEM

$$PEM\left(\vec{H}\left(\vec{X}_T(t)\,,\vec{X}_{E:f};\vec{\Theta}\right)\right) = \vec{Y}_{T,E:f}$$
$$PEM\left(\vec{H}\left(\vec{X}_T(t)\,,\vec{X}_{E:sp};\vec{\Theta}\right)\right) = \vec{Y}_{T,E:sp}$$

where the figure of merit $\Delta\vec{Y}_{T,E:sp-f}$ is the difference of the results given by

$$\Delta\vec{Y}_{T,E:sp-f} = \vec{Y}_{T,E:sp} - \vec{Y}_{T,E:f}.$$

These results will need to be compared with the uncertainty, as described earlier, to give distributions of the figure of merit for the mission profile $\vec{X}_T(t)$.

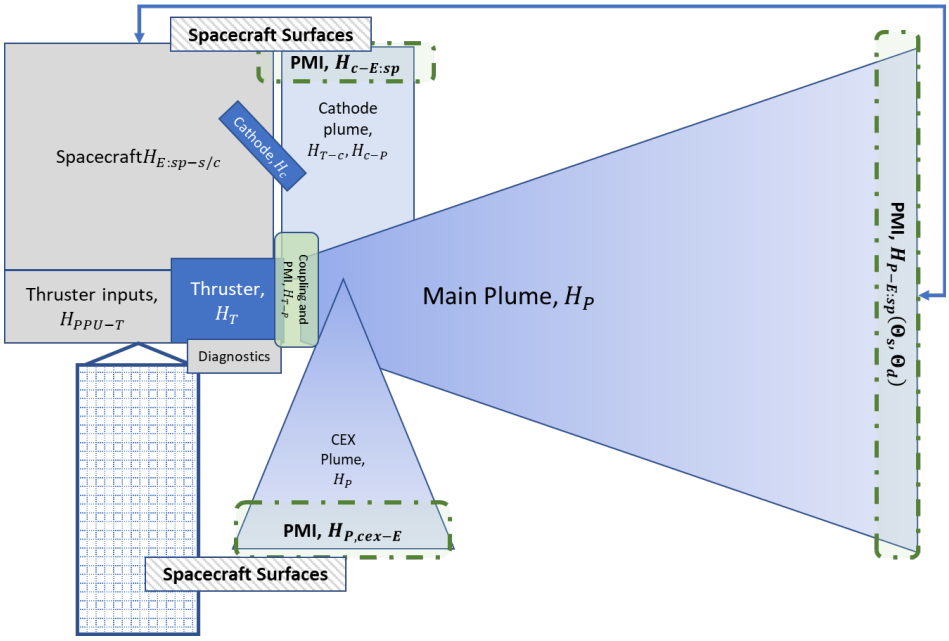

Figure 7: CV discretization of models as applied space operation of an EP device.

IV. PEM Example: Ion Thruster Life Modeling

An example of how the PEM can be used for thruster life and performance was originally performed for the NSTAR ion thruster by Wirz, et al. [2-5] using coupled ion thruster discharge, ion optics, and near plume models guided and validated by experimental data from multiple ground tests. A similar approach was later conducted with these ion optics models by Polk, et al. for the NEXT thruster [10]. The following summarizes the NSTAR life estimation effort and development of the model CEX2D-tebs by Wirz [2].

Excessive electron backstreaming through ion optics can end the effective life of an ion thruster, thus limiting the total ΔV achievable for a mission. Electron backstreaming (EBS) is caused by the random flux of high energy electrons from the thruster's beam that flow back into the discharge chamber by exceeding the potential barrier established by the accel grid. A schematic of this potential barrier is shown in Figure 8, which shows approximate axial potential traces at differing radial positions in the beamlet. It is important to minimize this effect since excessive backstreaming wastes valuable spacecraft power and impacts thruster life; therefore, an electron backstreaming fraction, f_{ebs}, limit of 1% is typically used for ion thrusters [refer to description of f_{ebs} in equation (5) below]. The minimum accel grid voltage

required to keep f_{ebs} below 1% is called the electron backstreaming voltage (or "limit"), $|V_{ebs}|$. For this condition, the Deep Space One (DS-1) flight spare NSTAR ion thruster used for the extended life test (ELT) lost the ability to run at full power (TH15) after processing 211 kg of xenon propellant due to $|V_{ebs}|$ values that exceeded the capability of the accel grid power supply [11]. A similar trend of increasing $|V_{ebs}|$ over time was observed during the original NSTAR 8200-hour Long Duration Test [12]. The following sections describe the CEX2D-tebs model, which is analogous to the approach that will be used by the PEM for ion thruster life estimation.

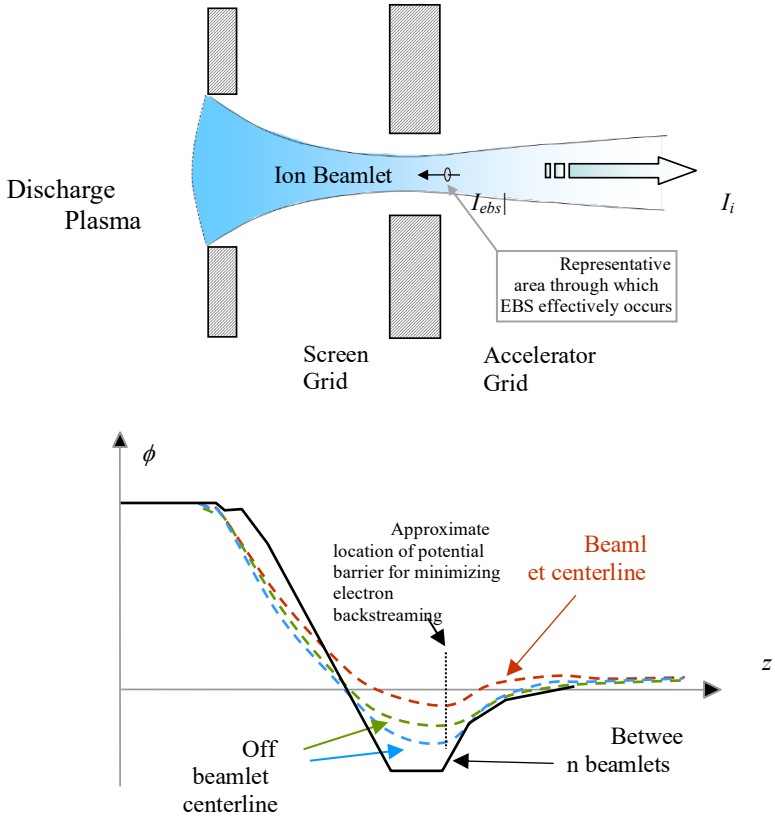

Figure 8. Schematic of an ion beamlet showing approximate potentials at different radial positions from beamlet axis and the small area through which electron backstreaming occurs.

A. Technique and Formulation

This section describes the electron backstreaming and grid erosion formulations for ion optics. The last part of this section describes how the CEX-2D-tebs model integrates these formulations and an ion optics code to provide self-consistent electron backstreaming and time dependent grid erosion results.

Electron Backstreaming Formulation

The $|V_{ebs}|$ determination technique described in this section can be used with any ion optics code that resolves the potential field along the beamlet. The following derivation shows how the electron backstreaming (EBS) current for a single beamlet is determined and then how this current is compared to the beamlet current to find the fraction of electron backstreaming for that beamlet.

Electron backstreaming is caused by the random flux of high energy electrons past the potential barrier established by the accel grid. The high energy electrons come from the tail of the thermal distribution of beam electrons. The retarding potential for each radial location for the gridlet (the minimum potential measured along the direction of the beamlet axis) occur near the accel grid aperture in the beamlet, resulting in a small area (pictured in Figure 8) in the center of the beamlet through which higher energy electrons can make their way back into the discharge chamber [13]. The electron backstreaming estimation method developed here assumes the electrons are nearly in thermal equilibrium; in addition, the electron drift, inertial, magnetic, and frictional forces are negligible such that the electron density, n_e, at a local potential, ϕ, is described by the Boltzmann relation

$$n_e(\phi) = n_{bp} \exp\left[\frac{\phi - \phi_{bp}}{T_e}\right] \tag{1}$$

where n_{bp}, is the average downstream beamlet density at the beam potential, ϕ_{bp}.

For ion thrusters, the accel grid sets up a potential barrier in the beamlet to prevent backstreaming of beam electrons. The flux of backstreaming electrons from the beam that will make it across a local potential minimum, ϕ_m, and back into the discharge chamber can be determined by using the Boltzmann relation from Equation (1). Since this relation determines the electron densities at local potentials as a function of the downstream beam plasma potential, ϕ_{bp}, and the beam plasma density, n_{bp}, the one-sided thermal flux of electrons for a local potential minimum, ϕ_m, can be integrated over the locus of minimum potentials created by the accel grid is found by searching along the beam axis at each radial location in the computational domain. The electron backstreaming current, I_{ebs}, for a gridlet is found by integrating the electron backstreaming flux over the surface defined by local minimum potentials, ϕ_m, such that

$$I_{ebs} = e\iint_S \Gamma_e dS = e\left(\frac{n_{bp}\bar{c}}{4}\right)\iint_S \exp\left[\frac{\phi_m - \phi_{bp}}{T_e}\right] dS \tag{4}$$

The parameters (i.e., n_{bp}, ϕ_{bp}, $\bar{c}$, and T_e) reflect downstream beam plasma conditions and are therefore constant across the integration surface. The backstreaming fraction, f_{ebs}, for a given domain (for example, a single gridlet or a given area of the extraction grids) is defined as the ratio of backstreaming electron current, I_{ebs}, to the outgoing ion current, I_i, such that

$$f_{ebs} \equiv \frac{I_{ebs}}{I_i} \tag{5}$$

During experimental efforts, this ratio is used to describe the backstreaming fraction for the entire beam by comparing the total beam current to the total EBS current throughout the beam. The value of this parameter is found by continually decreasing the magnitude of the accel grid voltage until a sharp rise in "measured" beam current indicates the beginning of prodigious electron backstreaming due to a decrease in the strength of the retarding potential near the accel grid apertures. The onset of EBS can defined as the voltage (i.e., the electron backstreaming voltage $|V_{ebs}|$) where $f_{ebs} \sim$ 1% for the entire beam. The computational method used by CEX2D-tebs for determining $|V_{ebs}|$ mimics the experimental technique by incrementally lowering the magnitude of the accel grid voltage until a specified value of f_{ebs} for the entire grid, or for certain gridlets, is exceeded. This method is attractive from a computational perspective since each new value of accel grid voltage uses the potential solution from the previous accel grid voltage to provide relatively fast potential solution convergence.

Erosion Prediction and Double Ions Correction

The CEX2D ion optics code [14] was modified to use the erosion rate information to reduce the mass represented by the computational nodes defining the grid until the node's mass is reduced to zero. Once a node's mass is eliminated, the geometry is modified accordingly and the ion optics code is then re-run to redefine the local potentials in the computational domain to determine the new beamlet characteristics in light of the new geometry. The new beamlet characteristics are then used to recompute the grid erosion rates until another node is eliminated. The grid geometry and remaining mass at each node are stored at the end of each iteration. This process is repeated until a predefined thruster operation time is reached. The user may define various operating conditions for a series of thruster operating times to simulate throttled operation such as demonstrated in the NSTAR ELT.

The NSTAR ion thruster uses xenon propellant and molybdenum ion optics grids. The sputter yields for xenon on molybdenum for normal incidence used in this effort were taken from references [15] and [16]. Yield curves were fitted to Rosenberg's data for $Xe^+ \rightarrow Mo$ incidence energies above 140 eV while the Doener's spectroscopic yield data was used for incidence energies below 60 eV. Rosenberg's and Doener's data were linearly averaged for normal incidence between 60 and 140 eV. The sputter yields used herein represent the nominal yield data; future efforts will include sensitivity analysis to assess the impact of the uncertainty in the yield data. At this time, all ion impacts are assumed normal to the grid surface; in future versions of the code we will use the technique for accounting for off-normal incidence as discussed in [14].

The double ion current ratio, γ, is used to correct the sputter yield and charge density values that contribute to plasma bombardment of the upstream face of the screen grid and direct impingement of other grid surfaces. Similarly, the erosion rate due to charge-exchange (CEX) ions is corrected for double ion content. The double ion current is also used to correct the space charge in Poisson's equation. The formulation to correct for the presence of double ions in CEX2D-tebs in described in detail in by Wirz [2].

Integrated Erosion and EBS Calculations using CEX2D-tebs

Analogous to the PEM, CEX2D-tebs combines grid erosion and $|V_{ebs}|$ determination to produce long-duration assessments of ion thruster life. A flow chart showing the interrelationship of the different components of the model is shown in Figure 9. The model is arranged such that simulations of ion optics erosion progress until a prescribed time, say "t_i", to find how the erosion of the grids will lead to modifications of the grid geometry. If a computational cell of grid material is completely eroded away, then it is considered that the grid geometry has effectively changed. At this point, the code then decides if sufficient time has passed (Δt_{min}) to execute a search for the EBS limit. A minimum time step for performing EBS limit, Δt_{min}, is used to prevent excessive runtimes for higher resolution runs, where the grid geometry can change frequently by small amounts. The code also checks to see if the stop time, t_i, has been reached; if so, the code progresses to the next thruster operating condition specified in "Input (i+1)"(at which time, an EBS limit determination is also conducted). At the next operating condition, the model uses the eroded grid geometry but can apply new values for parameters such as grid gap, beamlet current, grid voltages, etc. The technique for determining grid erosion and $|V_{ebs}|$ is discussed above.

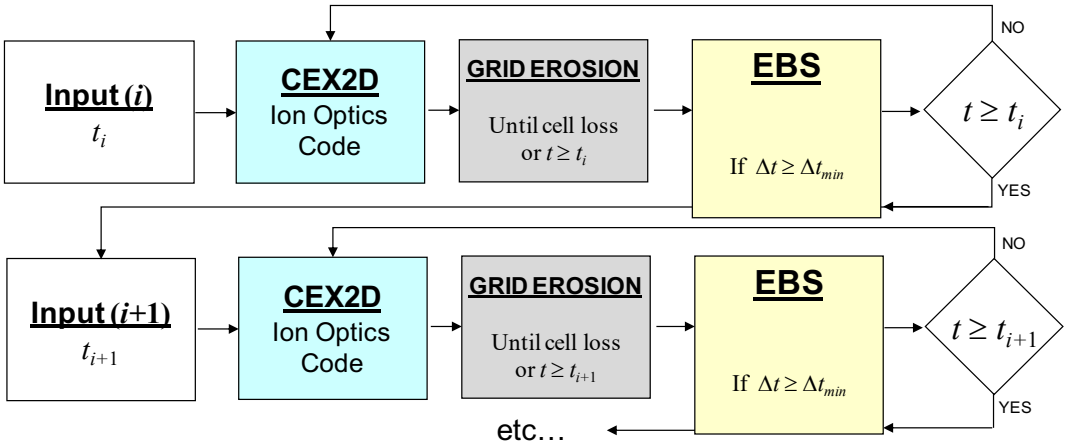

Figure 9. Flow Chart for CEX2D-tebs, showing how electron backstreaming is determined for eroded geometries during long duration analysis of ion optics operation.

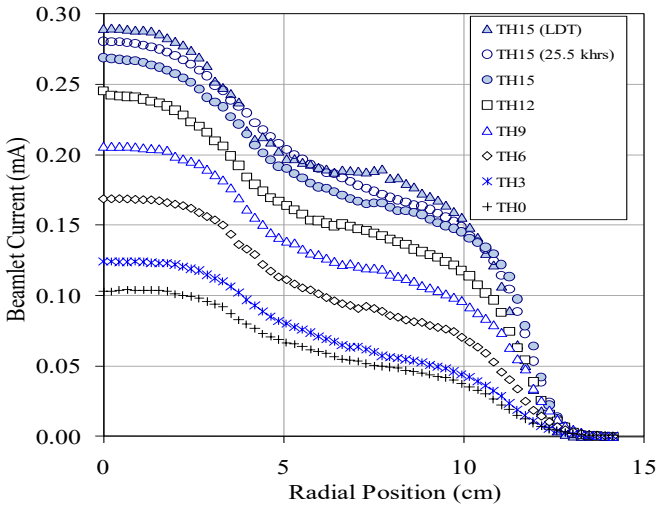

Figure 10. Beamlet current vs. radial position for the NSTAR ELT at various throttle conditions for beginning of life and for TH15 at 25.5 khrs. Also shown is the profile at the beginning of the NSTAR LDT.

B. Results

Parametric Analysis of Erosion Model

A simple parametric analysis of the equations from Section II-B provides an indication of the importance of considering double ions for grid erosion analysis. This analysis is not entirely self-consistent, but it provides a means to interpret the erosion estimates made by CEX2D-tebs for different double ion ratios. A basic diagram of the grids and grid erosion mechanisms is shown in Figure 11. The relative sputter yield for the impact of discharge ions of the upstream surface (using Y_{dc}) was analyzed assuming discharge ions hit the screen grid with energy equal to the discharge voltage; therefore, energy of 25 V was used for single ions. The sensitivity analysis for sputter yield due to charge exchange ions on the accel grid (using Y_{CEX}) was performed by assuming the singly-charged ion energy is the beam plasma potential minus the accel grid potential (i.e., for single ions the nominal case gives $\phi_{bp} - V_a = 15 + 180 = 195$ V; worst-case gives $\phi_{bp} - V_a = 15 + 260 = 275$ V).

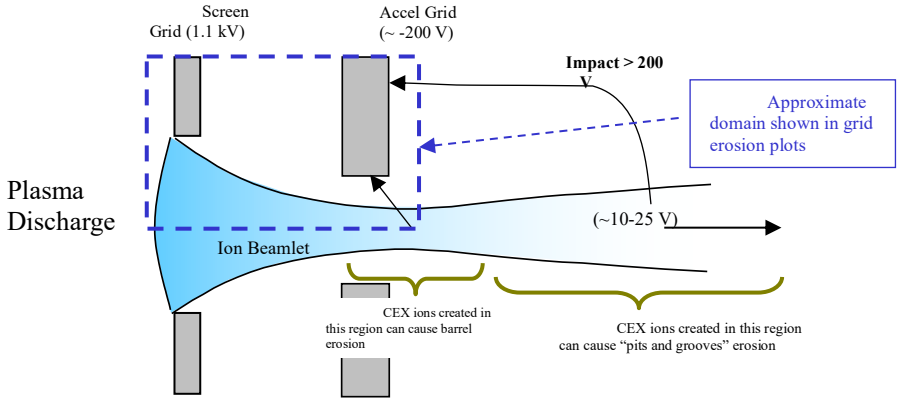

Figure 11. Diagram of CEX erosion mechanisms for a single beamlet. Also shown is the portion of the computational domain used to show CEX2D-t grid erosion estimates in later figures (note: entire computational domain extends 5 cm downstream).

The results of this simple parametric analysis are shown in Figure 12. These results show that an increased double ion ratio (which can be as high as 0.3 for NSTAR on centerline) significantly increases the direct sputter yield for the screen grid. The accel grid erosion due to charge exchange ions decreases for increasing double ion content due to the fact that the effective number of ions is reduced by a factor of two and the yield at double ion energy is less than twice that for single ions at the energies of interest; in addition, at these energies the ratio of the collision cross-sections for doubly- to singly-charged CEX ions is less than ½. The results also show that increased double ion content reduces charge density modestly, which is clear from the equations in the double ion formulation. These double ion effects proved to be important to accurately modeling grid erosion for the NSTAR thruster [17].

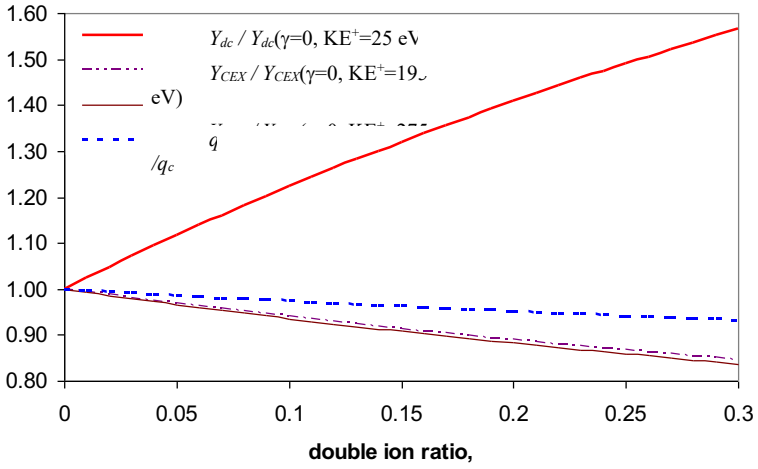

Figure 12. Sensitivity analysis of sputter yield and charge density vs. double ion ratio.

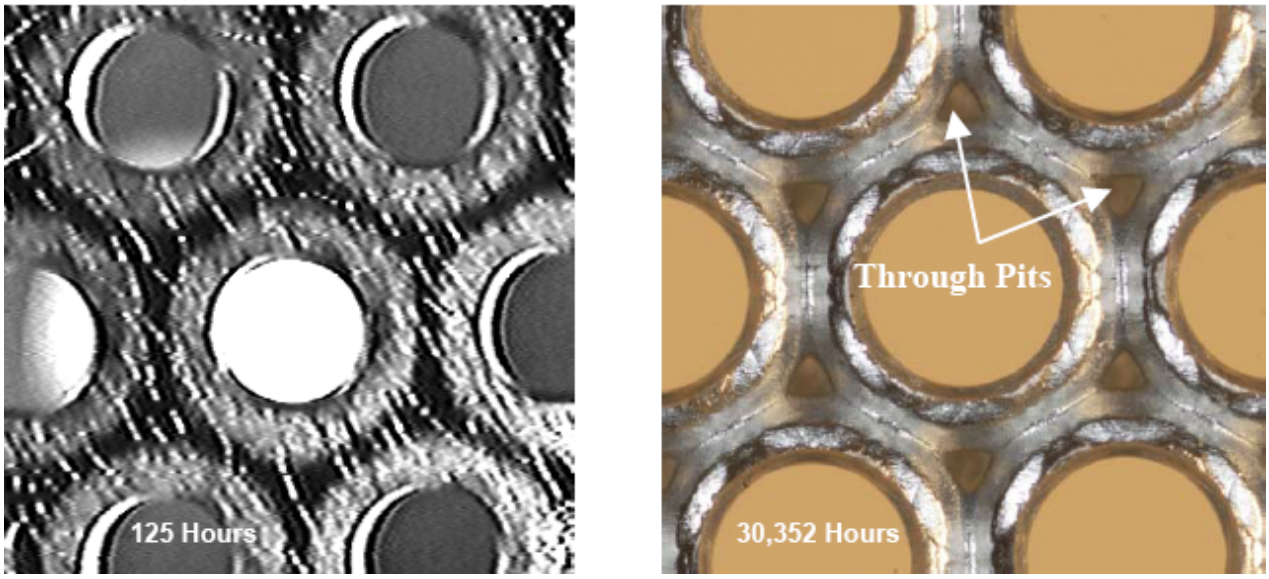

Figure 13. Downstream face of the NSTAR accel grid at the beginning and end of test.

The results of the erosion code show good agreement with both NSTAR LDT and ELT data. A picture of the downstream face and apertures of the accel grid as observed during the ELT is shown in Figure 13. Observed erosion of the grids during the LDT and ELT test data are shown by the purple and blue lines shown in Figure 14 (refer to Figure 11 to see the approximate domain used in the following figures for grid erosion profiles) . As shown in Figure 15, result for the erosion model for LDT conditions compare very well with these data. Similar agreement was seen for the ELT as shown in Figure 16 and discussed in [17].

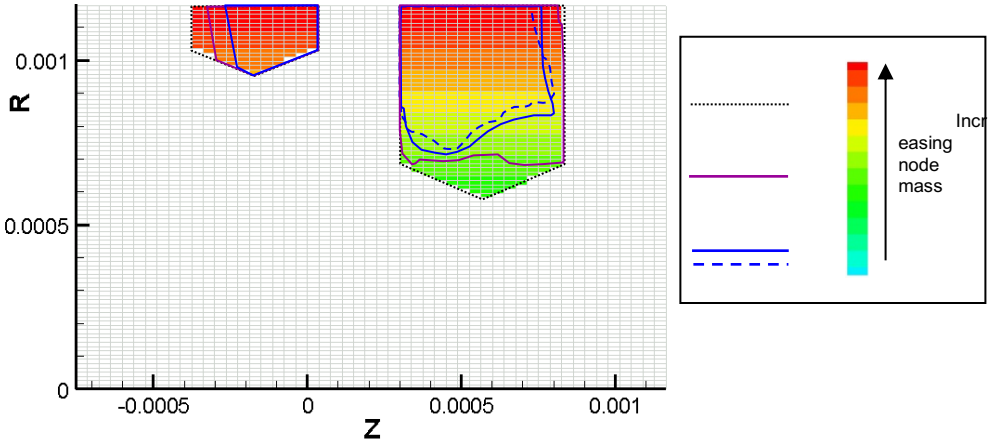

Figure 14. Beginning-of-Life (BOL) grid geometry at start of simulation. Computational grid in near-field is shown; however, mesh extends 5 cm downstream to include downstream CEX ions that contribute to erosion.

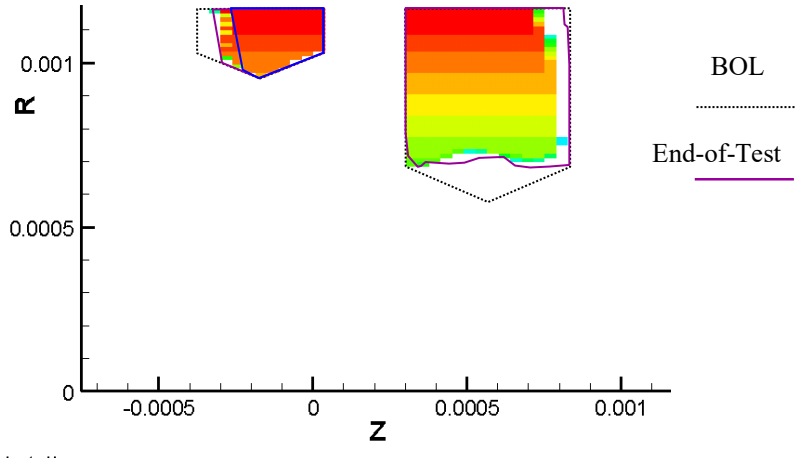

Figure 15. LDT erosion estimate after 8200 hours, compared with experimental profiles.

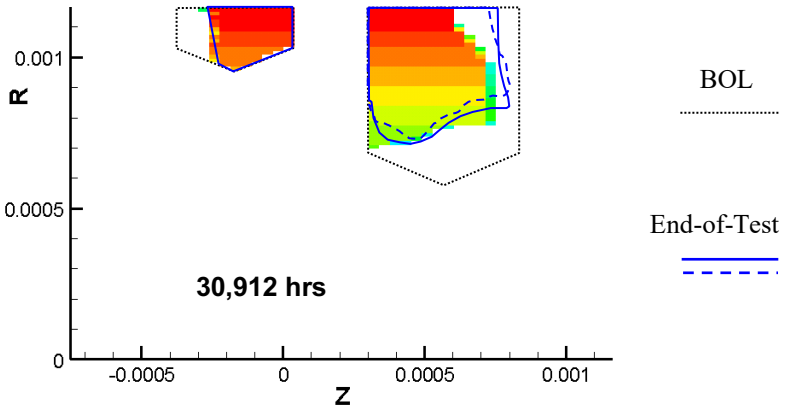

Figure 16. Comparison of erosion model with End-of-Test ELT measurements.

Inputs for Ion Optics Erosion and EBS Analysis

Input parameters used for the model were derived from experimental and computational results [11,12,17,18,19]. The beamlet currents used for the analysis below are shown in Figure 10. This figure also provides the NSTAR beamlet profiles for the full range of throttle conditions (TH0 – TH15) at the beginning of the ELT, for TH15 near the end of the ELT (25.5 khrs), and for the NSTAR 8200-hour LDT. The potential for the downstream beam plasma, ϕ_{bp}, and electron temperature, T_e, were nominally 10 V and 1.8 eV. The upstream electron temperatures and neutral densities for TH15 were taken from the values produced by the ion thruster discharge chamber model, DC-ION [20]. The grid gap for ion thrusters using two outwardly dished molybdenum grids, such as NSTAR typically reduces due to the differential thermal expansion of the screen and accel grid [18,22]. Therefore, the nominal hot grid gap (during thruster operation) used for the center hole at beginning of thruster life (at TH15) was the 0.30 mm spacing measured for TH15 in reference [18] (this assumes an initial cold grid gap of 0.66 mm and a lessening of the grid gap by 0.36 mm during thruster operation). For lower throttle conditions, nominal values for changes in hot grid gap of approximately -0.35 and -0.20 mm for throttle conditions TH8 and TH0 were used [18]. Since data on the radial variation of the hot grid gap is unavailable, this study assumes that the hot grid gap varies linearly from the minimum at the center of the grid to the cold grid gap value at the grid periphery. Post-test analysis for the ELT showed that the cold grid gap had changed approximately -0.19 mm. Previous analyses discussed in reference [13,21] and sensitivity analyses given below show that reduction of hot grid gap may explain sharp rises in the magnitude of the electron backstreaming later in thruster life.

Results from long-duration testing of the NSTAR thrusters showed that the center region of the grids experienced the significant erosion and accel grid aperture enlargement [11,12,19]. Preliminary computational analysis showed that these features lead to increased electron backstreaming [13,17]. As discussed below, the erosion and $|V_{ebs}|$ analysis is primarily conducted at the center gridlet/beamlet since the highest beamlet current, most significant erosion, and smallest grid gap occur in the center region of the NSTAR grids [22]. As a result, the most significant changes to grid geometry and electron backstreaming occur in this region, thus dictating the $|V_{ebs}|$ trend for the entire grid.

EBS determination

Electron backstreaming was determined for the NSTAR profiles shown in Figure 10, for which the beamlet currents were calculated from ELT Faraday probe traces using the technique discussed in reference [11]. Using these beamlet densities and the formulation from Section A, it was found that the potential barrier is essentially just upstream of the accel grid for most configurations. Integrating equation (4) over this potential barrier for several single beamlets it was found that over 99% of the electron backstreaming occurs in a small area that is less than 20% the size of the beamlet at this location. This concentration of electron backstreaming current can be seen from plots of the electron backstreaming current density versus beamlet radius, as shown in Figure 17. This plot is indicative of the electron backstreaming conditions in the beamlet for all conditions examined.

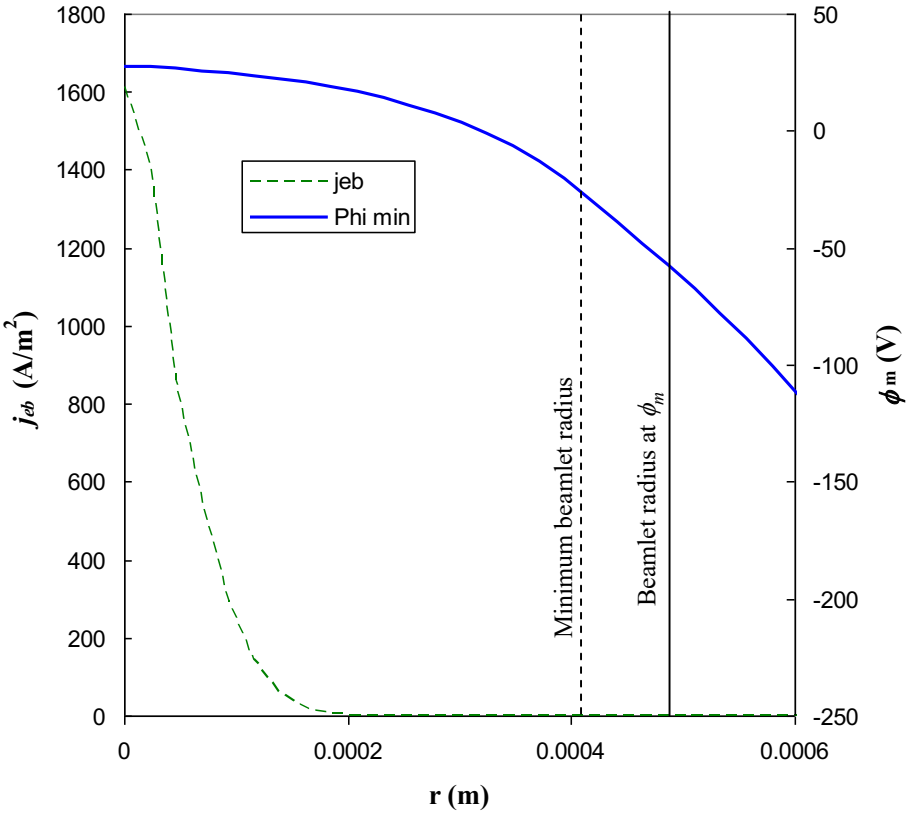

Figure 17. Electron backstreaming current density, j_{eb}, and minimum potential, ϕ_m, vs. beamlet radius for TH15 at ELT end of test condition for center beamlet. (Note: the minimum beamlet radius is typically found just upstream of the accel grid while the minimum potential is typically just downstream of the accel grid)

For NSTAR experiments, the fraction of electron backstreaming, f_{ebs}, for determining $|V_{ebs}|$ was set at 1%. In an effort to understand how the electron backstreaming varies over the radial extent of the grids, the CEX2D-tebs model was used to find f_{ebs} for several apertures along the NSTAR grid radius. For the beam profiles in Figure 10 it is reasonable to use trapezoidal integration between radii 0, 2, 4, 6, 8, 10, and 13 cm to determine the backstreaming limit for the entire beam. The "local f_{ebs}" values at these radial locations are given in

Figure 18 for the condition where f_{ebs} = 1% for the entire beam. In general, for the NSTAR beam profiles at all throttle conditions it was found that a local value of $f_{ebs} \approx 10\%$ for the center hole corresponds to a "total f_{ebs}" of 1% for the entire beam. It was also found that over 99% of the backstreaming current occurs inside of r = 6 cm of the over 28 cm diameter NSTAR grids. Based on these results, an electron backstreaming limit condition of $f_{ebs} \approx 10\%$ for the center gridlet was used in the following analyses. As discussed below, inspection of the nearly vertical shape of the $|V_{ebs}|$-curves above 10% (such as those in Figure 19) reveals that specifying this condition anywhere above 10% will change the $|V_{ebs}|$ result by only about one volt or less.

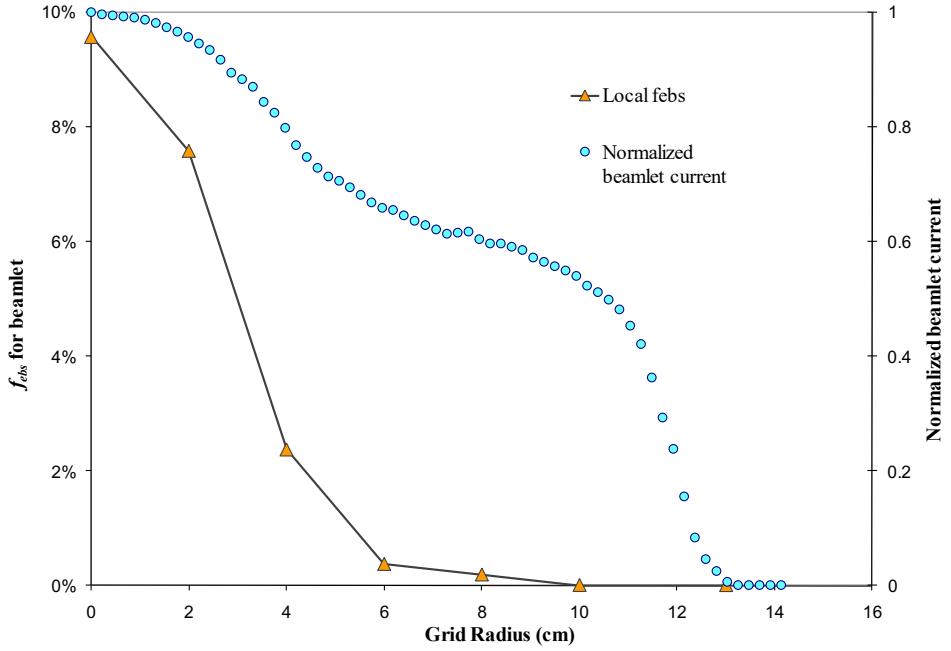

Figure 18. Local f_{ebs} values across a normalized NSTAR beam.

Figure 19 shows example $|V_{ebs}|$-curves generated by CEX2D-tebs for the NSTAR 8200-hour Long Duration Test (LDT) for a single gridlet using the method discussed in Section A using 1-volt increments in accel grid voltage. These data are similar to the $|V_{ebs}|$-curves used throughout this effort. Also, these data are plotted on two ranges for the *y*-axis for clarity and to show that specifying the beam f_{ebs} at values above 10% will change the results very little.

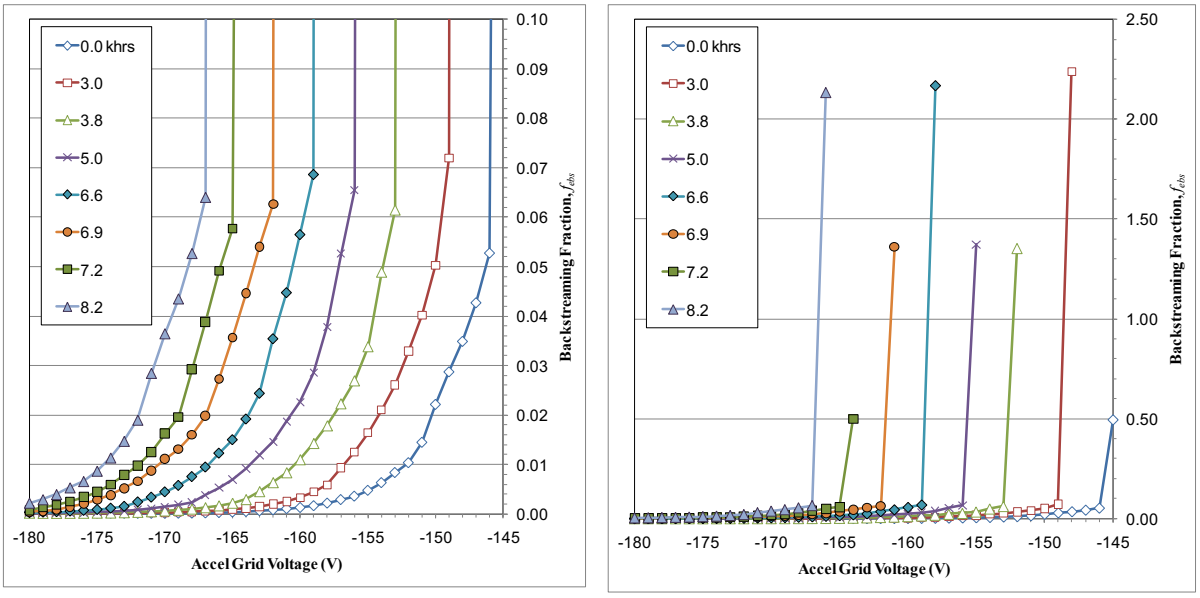

Figure 19. Typical $|V_{ebs}|$-curves for the NSTAR 8200 Long Duration Test for a single gridlet at different run times in khrs. These data are plotted on two different axes for f_{ebs} for clarity.

Comparison of CEX2D-tebs results with LDT data

Using the method discussed above, the CEX2D-tebs model was run for the conditions during the NSTAR LDT and

ELT long duration tests. For the LDT, the model was run at TH15 for 8200 hours at the conditions described in [12] and discussed above. The trend of $|V_{ebs}|$ values vs. runtime are compared to the LDT data in Figure 20 and show good agreement for a grid gap of l_g = 0.30 mm. Improved agreement is found for a grid gap of l_g = 0.34 mm. This gap is reasonable since the NSTAR LDT thruster is not the same thruster as the NSTAR engineering model used for the measurements in reference [12]. Therefore, it is possible that the grid gap for the two thrusters differs by 40 microns, a difference of about 13%, or that these values are within the error of the measurements. An interesting trend that is evident in this plot is that, for these conditions, the larger grid gap starts at a lower $|V_{ebs}|$ but causes a steeper rise in magnitude. By examining the erosion rates for the conditions in Figure 20, it is clear that the larger grid gap results in slightly faster erosion of the accel grid aperture, thus leading to the different rate of change in $|V_{ebs}|$ shown in the plot.

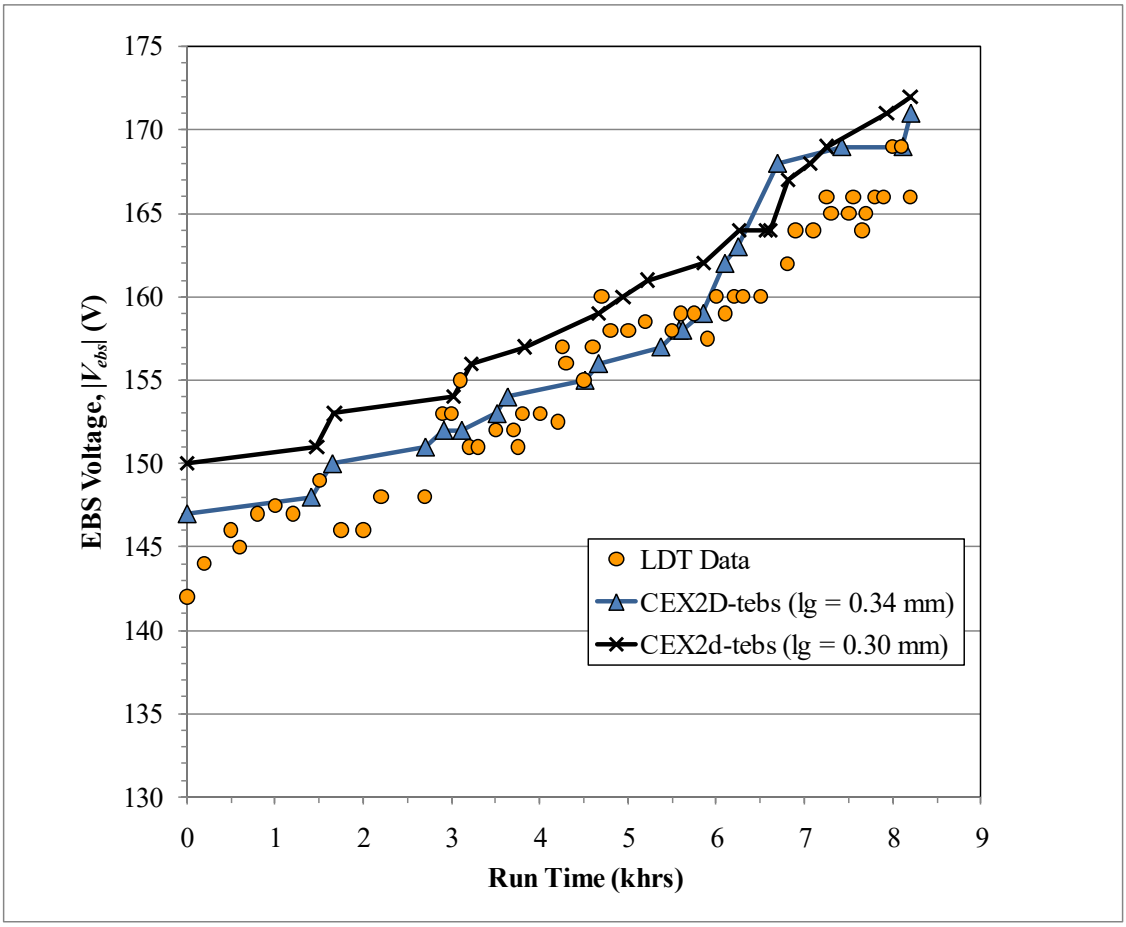

Figure 20. CEX2D-tebs results compared to LDT Data for two different grid gap, l_g, values.

Comparison of CEX2D-tebs results with ELT data

One of the major advantages of CEX2D-tebs is the ability to allow the user to specify the grid gap at any time during the thruster operation. Changes in grid gap can be caused by different operating conditions or changes due to grid erosion [18,22,**Error! Bookmark not defined.**]. During the NSTAR ELT, the thruster was run at multiple throttle levels during the over 30 khrs of operation. During this test, the grids experienced significant erosion and a decrease in the cold grid gap was measured during post-test analysis [19]. As discussed in reference [21], a decrease in grid gap helps explain the $|V_{ebs}|$ trends observed during the NSTAR ELT. Consequently, a few different trends in grid gap were analyzed to examine the effect of decreasing grid gap on the accuracy of $|V_{ebs}|$ values in comparison to ELT data. By comparing the grid gaps from Table 1 and the corresponding CEX2D-tebs results in Figure 21 it is clear that good agreement can be achieved if a decreasing grid gap is considered. Comparing the results from Run 1 and Run 2 shows that if the grid gap at the beginning of the test is 0.34 mm instead of 0.30 mm, similar to the LDT results, some improved agreement with the data during later Test Segments is found. The best agreement with end of test and maximum $|V_{ebs}|$ (which can signify end of thruster life) occurs with a gradual change in the grid gap for TH15 as shown in Run 3; however, this scenario does not reproduce the sharp rise seen during Test Segment 5. The results shown here specify a constant grid gap during each Test Segment.

As discussed below, future efforts will investigate the possibility of gradual grid gap changes during each Test Segment.

Table 1. Input Sets (Run 1, Run 2, and Run 3) for ELT Simulations

Test Segment	Throttle Level	Grid Gap (mm)		
		Run 1	Run 2	Run 3
1	TH15	0.30	0.34	0.34
2	TH8	0.34	0.34	0.34
3	TH15	0.25	0.25	0.3
4	TH0	0.45	0.45	0.45
5	TH15	0.25	0.25	0.25
6	TH5	0.25	0.25	0.25

These data also include an increase in beamlet current at the center gridlet over the life of the test for TH15 of about 4.5% after 25.5 khrs, as shown in Figure 10. The increase in beamlet current was assumed to grow gradual over the life of the test to the value given for the TH15 condition at 25.5 khrs. To show the effects of including increasing beamlet current, "Run 4" was conducted with the same conditions as Run 1, except *without* increasing beam current. A comparison of Run 1 and Run 4 in Figure 22 shows that increasing beamlet current helps capture the steep rise in $|V_{ebs}|$ during Test Segment 5 and the $|V_{ebs}|$ values during Test Segment 6.

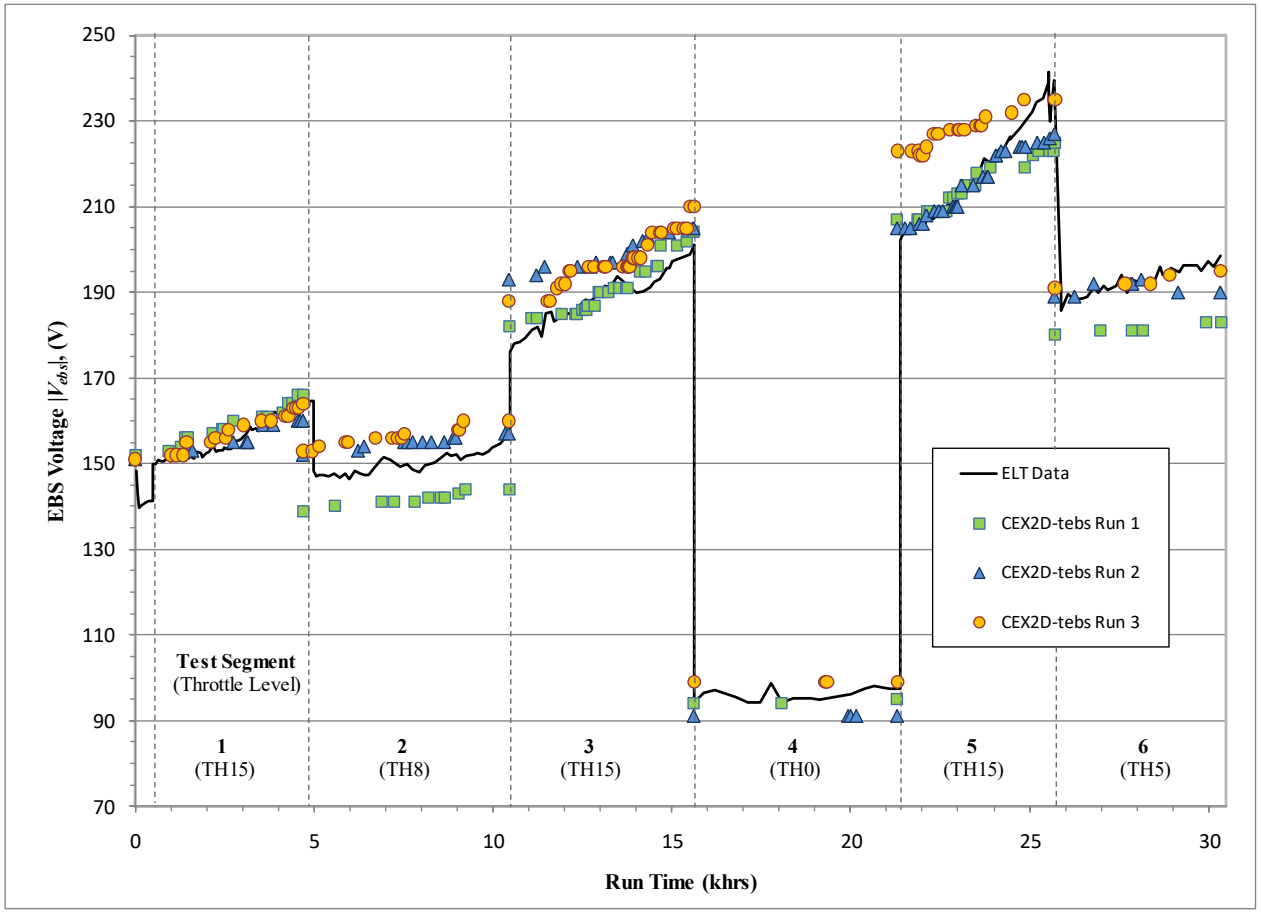

Figure 21. Comparison of CEX2D-tebs results for Runs 1, 2, and 3 with data from ELT.

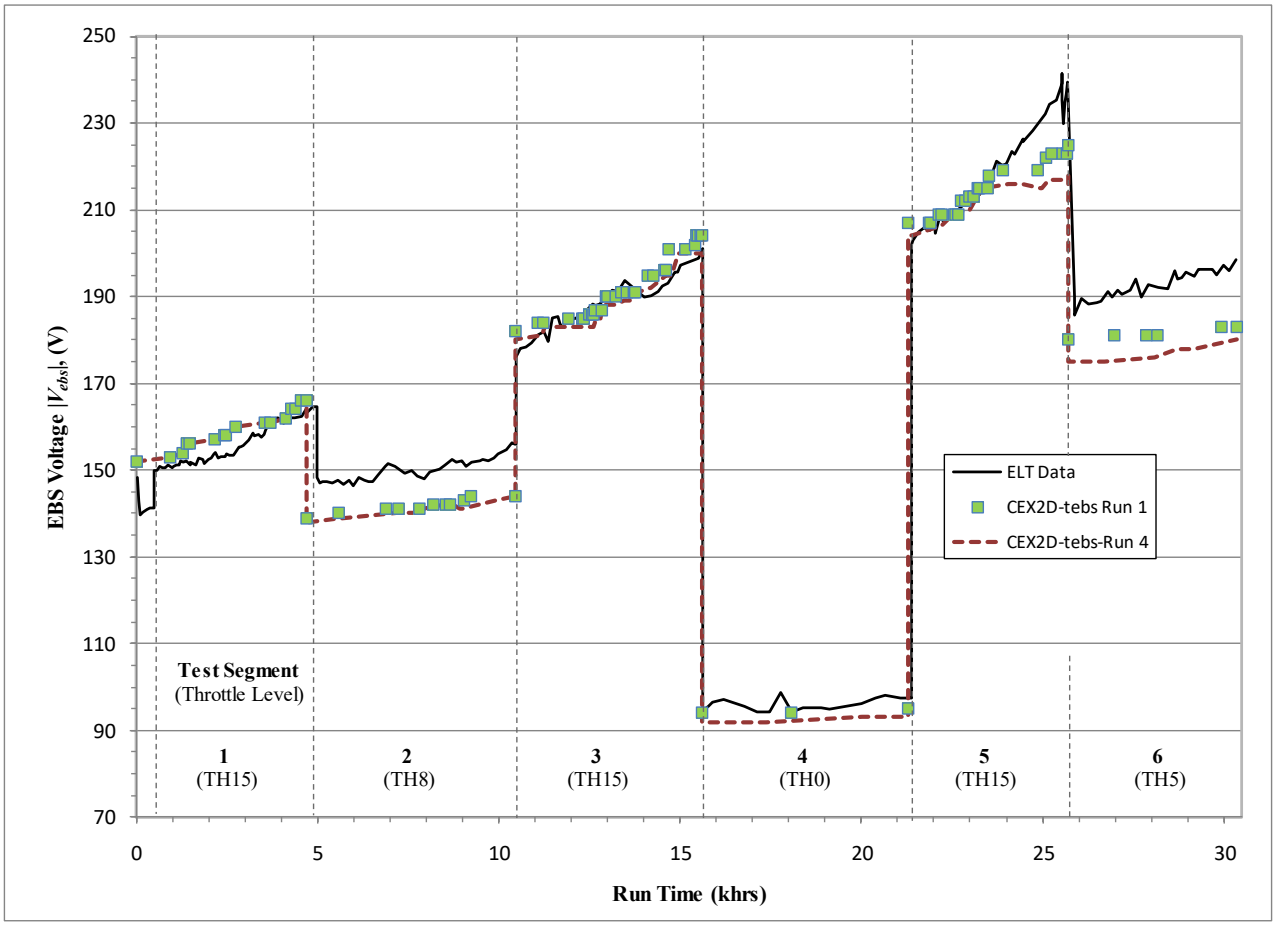

Figure 22. Comparison of CEX2D-tebs results for changing beamlet current. Run 4 is identical to Run 1, except without increasing nominal beamlet current during the test.

C. Takeaways from the CEX2D-tebs effort

CEX2D-tebs provides useful and accurate assessments of long duration electron backstreaming for ion optics operating for long durations. The results from this paper show that CEX2D-tebs provides useful and accurate assessments of long duration electron backstreaming for ion optics operating for long durations. By integrating electron backstreaming current over the thruster beam it was found that over 99% of the backstreaming current occurs inside of $r = 6$ cm for the over 28 cm diameter NSTAR grid. Additionally, a value of $f_{ebs} = 10\%$ for the center gridlet corresponded to $f_{ebs} \sim 1\%$ over the entire beam. Consequently, a nominal value of $f_{ebs} = 10\%$ was used for the center gridlet to reflect $f_{ebs} \sim 1\%$ for the entire thruster. Analysis of the $|V_{ebs}|$-curves suggests that any reasonable value above 10% for the center gridlet should change the $|V_{ebs}|$ by only about one volt. The CEX2D-tebs model agrees well with $|V_{ebs}|$ data from the long duration NSTAR tests, LDT and ELT. The best agreement for the LDT and ELT was found for an initial grid gap slightly larger than that measured in experimental test. The results further substantiate claims from previous analysis that suggests that decreasing grid gap, in addition to grid erosion, largely explains the steep rises in $|V_{ebs}|$ observed during the NSTAR ELT. Improved agreement with the ELT results is also found by including the effects of increasing center beamlet current with time, as was observed during thruster testing. For the PEM model, CEX2D-tebs would work with other models to account for facility effects, UQ, and considerations of the space environment.

V. Conclusions and Future Work

Predicting high-power thruster in-space performance from ground testing presents a considerable challenge for JANUS researchers. The PEM framework provides an organized and useful approach to high-power EP life and performance estimation with UQ for probabilistic extrapolation and feedback to the institute efforts. To allow effective integration between the many JANUS investigation, the PEM will utilize a control volume (CV) approach to allow researchers to interact at the boundaries of their domain. Predicting ion thruster life with CEX2D-tebs provides a useful example of how the PEM framework and CV approach can use multi-scale, multi-physics, and multi-fidelity models to integrate with other models and experimental efforts to account for facility effects, UQ, and the space environment.

VI. Acknowledgements

This work was funded by Joint Advanced Propulsion Institute 20-STRI-FULL-0004, NASA Grant Number 80NSSC21K1118.

VII. References

[1] Mitchell Walker, Dan Lev, Benjamin Jorns, John Foster, Alec Gallimore, Alex Gorodetsky, Joshua Rovey, Huck Beng Chew, Deborah Levin, John Williams, Azer Yalin, Richard Wirz, Jaime Marian, Iain Boyd, Kentaro Hara, Kristina Lemmer, "Overview of the Joint AdvaNced PropUlsion InStitute (JANUS)," IEPC-2022-156, 37th International Electric Propulsion Conference, Boston, Massachusetts, June 19-23, 2022.

2 Wirz, R. E., "Coupled Analysis of Ion Thruster Grid Erosion and Electron Backstreaming," Space Propulsion 2010, San Sebastian, Spain, May 2010.

3 Wirz, R. E., "Long Duration Assessment of Electron Backstreaming for Ion Optics," IEPC-2009-164, 31st International Electric Propulsion Conference, Ann Arbor, MI, USA, September 2009.

4 Wirz, R. E., Anderson, J., Katz, I., "Time-Dependent Erosion of Ion Optics," Journal of Propulsion and Power, Vol. 27, No. 1, Feb. 2011, pp. 211-217.

5 Wirz, R. E., Katz, I., Goebel, D., Anderson, J., "Electron Backstreaming Determination for Ion Thrusters," Journal of Propulsion and Power, Vol. 27, No. 1, Feb. 2011, pp. 206-210.

6 Yim, J. T., "A survey of xenon ion sputter yield data and fits relevant to electric propulsion spacecraft integration," IEPC-2017-060, 35th International Electric Propulsion Conference, Atlanta, GA, October 8-12, 2017.

7 Gorodetsky, A. A., Jakeman, J. D., Geraci, G., Eldred, M. S., "MFNETS: multifidelity data-driven networks for Bayesian learning and prediction," International Journal of Uncertainty Quantification, 2020. – Accepted.

8 Gorodetsky, A. A., Geraci, G., Eldred, M. S., Jakeman, J., "A generalized approximate control variate framework for multifidelity uncertainty quantification," Journal of Computational Physics, Vol. 408, 2020, 109257.

9 Jakeman, J., Eldred, M. S., Geraci, G., Gorodetsky, A. A., "Adaptive multi-index collocation for uncertainty quantification and sensitivity analysis," International Journal for Numerical Methods in Engineering, Vol. 121, 2019, pp. 1314 – 1343.

10 Polk J. E., et al. "Modeling ion optics erosion in the NEXT ion thruster using the CEX2D and CEX3D codes," IEPC-2019-907.

11 Brophy J. R., "Propellant Throughput Capability of the DAWN Ion Thrusters," IEPC-2007-279.

12 Polk J. E., et al, "An Overview of the Results from an 8200 Hour Wear Test of the NSTAR Ion Thruster," AIAA-99-2446, 35th AIAA/ASME/SAE/ASEE Joint Propulsion Conference and Exhibit, 20-24 June 1999, Los Angeles, California.

13 Wirz R., Katz I., Goebel D., Anderson J., "Electron Backstreaming Determination for Ion Thrusters," AIAA-2008-4732.

14 Brophy J. R., Katz I., Polk J. E., Anderson J. R., "Numerical Simulations of Ion Thruster Accelerator Grid Erosion," AIAA 2002-4261.

15 Doerner, R. P., Whyte, D. G., and Goebel, D. M., "Sputtering Yield Measurements During Low Energy Xenon Plasma Bombardment," *Journal of Applied Physics*, Vol. 93, No. 9, May 2003, pp. 5816-5823.

16 Rosenberg, D., and Wehner, G. K., "Sputtering Yields at Very Low Energy He+-, Kr+-, and Xe+- Ion Bombardment," *Journal of Applied Physics*, Vol. 33, No. 7, 1962, pg. 1824.

17 Wirz R., Anderson J., Katz I., Goebel D., "Time-Dependent Erosion of Ion Optics," AIAA-2008-4529

18 Diaz E. M., Soulas G. C., "Grid Gap Measurement for an NSTAR Ion Thruster," NASA/TM-2006-214249, IEPC-2005-244
19 Anderson J. R., et al, "Post-Test Analysis of the Deep Space One Spare Flight Thruster Ion Optics," AIAA 2004-3610.
20 Wirz R., Katz I., "Plasma Processes of DC Ion Thruster Discharge Chambers," AIAA 2005-3690, *41st Joint Propulsion Conference*, Tucson, AZ, 2005
21 Wirz R., "Long Duration Assessment of Electron Backstreaming for Ion Optics," IEPC-2009-164, Presented at the 31st International Electric Propulsion Conference, University of Michigan • Ann Arbor, Michigan, USA, September 20 – 24, 2009
22 Soulas G. C., "Calculation of Thermally-Induced Displacements in Spherically Domed Ion Engine Grids," IEPC-2005-248, *Presented at the 29th International Electric Propulsion Conference, Princeton University, October 31 – November 4, 2005*